SMOS: A streamlined model-based optimization approach for super-resolution ultrasound localization microscopy

Xuan-Hieu Le, Denis Kouame, Duong-Hung Pham

SMOS: A Streamlined Model-Based Optimization Approach for Super-Resolution Ultrasound Localization Microscopy

Xuan-Hieu Le, Denis Kouamé, and Duong-Hung Pham

***Abstract*—Ultrasound Localization Microscopy (ULM) represents a significant advancement over conventional ultrasound (US) imaging, for reconstructing microvascular structures with micrometer-scale precision. However, existing model-based ULM approaches often rely on a complex five-step processing framework, which complicates parameter tuning and tissue signal suppression. Additionally, many of these methods either insufficiently account for the point spread function (PSF) - thereby compromising the accuracy of the final reconstruction - or are computationally intensive. While end-to-end data-driven methods show promise, they often require substantial training data and reliable ground-truth annotations. In this study, we introduce a novel approach named Streamlined Model-Based Optimization Approach for Super-Resolution Ultrasound Localization Microscopy (SMOS) which addresses these limitations. Our method improved the existing ULM process by replacing the first three steps with a single unified model. Experimental results on both *in silico* and *in vivo* datasets demonstrate the enhanced performance of our approach compared to existing benchmarks.**

***Index Terms*—Super Resolution, Microbubbles, Ultrasound Localization Microscopy, Inverse Problem, RPCA.**

I. Introduction

Ultrasound (US) has long been one of the most cost-effective and popular tools for medical diagnostics. However, its spatial resolution is fundamentally constrained by several physical factors such as wave diffraction or attenuation [1]. By leveraging the interaction between sparse US contrast agents-such as microbubbles (MBs) - and ultrafast imaging techniques, the recent advent of ultrasound localization microscopy (ULM) enables the visualization of clinically significant microvascular structures with sub-wavelength precision and high sensitivity [2]. Despite its advantages, ULM still faces a significant trade-off between acquisition time and reconstruction accuracy [3]. Specifically, a lower concentration of injected MBs ensures clear separation and obviously recognizable MB signals, thereby enhancing image reconstruction quality. However, this benefit comes at the cost of requiring a larger number of frames for sufficient localization to populate the vessel space, thus increasing acquisition time. In contrast, higher MBs concentrations are theoretically encouraged for reducing acquisition time and easing the data collection, as fewer frames are needed to achieve vascular coverage [4]. However, this leads to significant spatial overlap of signals, complicating detection and degrading localization accuracy. Addressing the challenge of maintaining high image quality under high MB concentration is therefore a critical research focus. Existing approaches to this challenge generally fall into two categories: model-based and data-driven methods. Model-based methods usually rely on a technical ULM pipeline including five steps as visualized in Figure 1: (1) tissue filtering, (2) MB detection, (3) sub-wavelength MB localization, (4) MB tracking, and (5) ULM image rendering [4]–[6].

In the first stage, tissue filtering, a widely adopted strategy involves applying Singular Value Decomposition (SVD) to the spatiotemporal Casorati matrix[1], to remove high-energy components predominantly attributed to tissue signals [5], [8]. However, the performance of SVD-based filtering depends heavily on an exhaustive manual selection of spectral thresholds. To overcome this, alternative methods such as Robust Principal Component Analysis (RPCA) and its variant - Deconvoluted RPCA (DRPCA) - have been introduced [9]–[11]. These approaches leverage the intrinsic sparsity of microvascular structures and have demonstrated improved performance in tissue suppression across various studies.

In the second stage, standard approaches typically assume that MBs produce locally high intensity peaks, which can be readily detected [5]. However, this assumption may not hold in practice, as MB signal intensity can sometimes be lower than background. As an alternative, [6] proposed a novel MB detection method based on the Neyman–Pearson (NP) criterion. It leverages statistical decision theory to enhance sensitivity to low-intensity MBs while maintaining control over false alarm rates. Nonetheless, this approach may lead to inaccurate reconstructions in high MB concentration scenarios.

The third stage, MB localization, has also been extensively explored, with the goal of achieving sub-wavelength resolution. Prominent representatives include interpolation-based method (e.g. Spline or Lanczos interpolation), Weight Average (WA) and Radial Symmetry (RS) [5]. Among these, RS has demonstrated superior robustness and effectiveness, making it one of the most reliable localization techniques. However, these existing approaches rely on complex localization algorithms while treating each step independently [5], [6] - leading to error accumulation and suboptimal results.

More recently, a computational Super-resolved Robust Principal Component Analysis (SRPCA) approach introduced in [12] extends the DRPCA [13] framework by replacing the first three steps of the traditional pipeline with a sequential process: bicubic interpolation of the input signal, followed by DRPCA applied to the upsampled data. While SRPCA

This version was submitted for review on May 31, 2025. This research is supported by the French National Research Agency (ANR) SONATINE project with grant number ANR-23-CE45-0002-01. The code of this paper is available at: *https://gitlab.irit.fr/minds/theseeric/smos*.

X.-H. Le, D. Kouamé and D.-H. Pham are with the IRIT Laboratory, Université de Toulouse, and CNRS, Toulouse 31400, France. (Corresponding author email: Hieu.Le-Xuan@irit.fr).

[1]The Casorati matrix is formed by vectorizing each frame of the acquired 3D US data and stacking them as individual columns of the matrix, as described in [7].

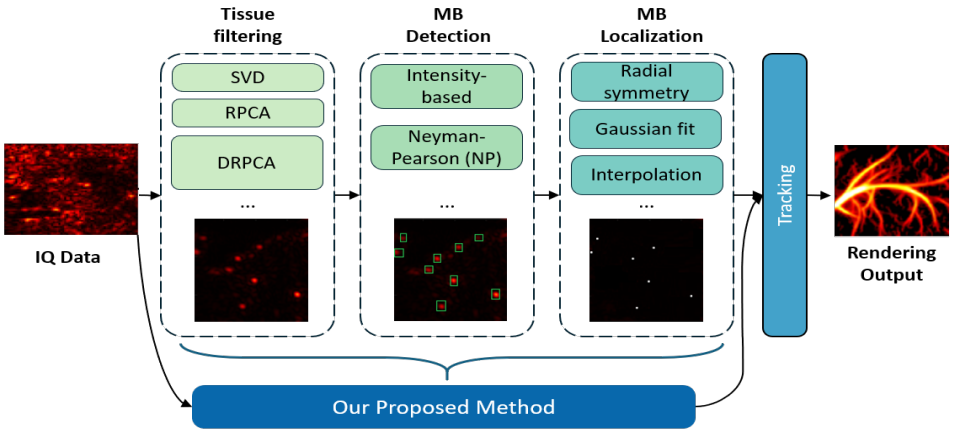

Fig. 1: Overview of a classical ULM pipeline with representative methods at each stage [5]. Our proposed algorithm SMOS replaces the first three steps, offering practical simplification benefits.

demonstrates significant improvements over RS-ULM across various datasets, it has several limitations. First, the interpolation step substantially increases computational cost due to the higher-dimensional input for DRPCA. Second, SRPCA does not support blind deconvolution, as it requires manual extraction of a single MB to serve as the PSF, thereby adding complexity to the process.

Data-driven approaches, mainly deep learning (DL) models, such as mSPCN [14] or RF-ULM [15], leverage convolutional neural network architectures trained and fine-tuned to directly predict subpixel MB localization. These methods show considerable promise in significantly reducing inference time. However, despite their growing popularity, DL-based approaches rely on simulated training data, which are generally not realistic. Generalizability and interpretability are also concerns, as models frequently require retraining for each new dataset, and achieving transparent model interpretability remains difficult due to their inherent end-to-end nature.

In response to these limitations, our earlier work - presented at ICIP 2025 [16]-introduced an method called the Blind Super-Resolved RPCA-Based Approach for Enhancing Blood Flow Estimation (BSRPCA). This method, representing a proof-of-concept of our proposed framework, was only demonstrated with limited preliminary results. In this paper, we introduce a comprehensive and detailed exposition of the algorithm, incorporate extensive validation across a wider range of comparative methods and datasets, and present a thorough comparative study accompanied by in-depth analysis. The contributions of this work are twofold:

- **First**, we introduce SMOS, an unified model-based approach that offers both conceptual and technical innovation by jointly addressing tissue filtering, MB detection, MB localization, and estimation of the system PSF for blind super-resolution in ULM. To the best of our knowledge, SMOS is the first unsupervised work to integrate all these key components into a single optimization framework. This integration significantly simplifies the ULM processing pipeline by reducing the number of discrete steps, minimizing the need for extensive parameter tuning, eliminating dependence on complex localization algorithms, and limiting error accumulation across stages.
- **Second**, through extensive experiments on both *in silico* and *in vivo* datasets, we demonstrate that SMOS achieves state-of-the-art performance, surpassing several recent methods such as those proposed in [5], [6]. Compared with SRPCA, our proposed SMOS yields comparable or superior results across many scenarios, while significantly reducing computational complexity. Finally, unlike DL-based methods, our approach does not require tailored simulation training data, thereby offering enhanced generalizability and greater interpretability.

II. Methodology

The main objective of our proposed approach, SMOS, is to unify and replace the first three steps of the traditional ULM pipeline - namely tissue filtering, MB detection, and sub-wavelength MB localization. By reformulating these tasks as a unified super-resolution problem, as illustrated in Figure 1, SMOS provides a cohesive algorithmic framework. To this end, we begin this section by outlining the problem formulation, followed by a detailed introduction of our proposed methodology.

For clarity and ease of reference, we provide, in Table I, a summary of the mathematical notations frequently used throughout the paper, along with brief descriptions. Additional context and detailed explanations are provided at the point of first use within the main text.

Notation	Description
z	A scalar variable
$\boldsymbol{z}$	A vector
$\boldsymbol{Z}$	A matrix
$\boldsymbol{Z}^H$	The conjugate transpose of $\boldsymbol{Z}$
I_N	Identity matrix of dimension N
$\mathbf{Soft}_\lambda(\boldsymbol{w})$	Soft-thresholding operator applied to $\boldsymbol{w}$ with threshold λ
$\mathbf{F}$	Unitary 3D Fourier transform matrix
$\mathbf{\Lambda}$	Diagonal matrix whose elements are the 3D Fourier transform of the zero-padded PSF
$\underline{\mathbf{\Lambda}}$	Defined as $\left[\left(\mathbf{1}_{dc}^T \otimes \mathbf{I}_{N_t}\right) \otimes \left(\mathbf{1}_{dr}^T \otimes \mathbf{I}_{N_z N_x}\right)\right] \mathbf{\Lambda}$.
1_w^T	Row vector of ones with dimension w.
SVD($\boldsymbol{w}$,r)	Partial singular value decomposition of $\boldsymbol{w}$ retaining the first r components

TABLE I: Summary of used mathematical notations.

A. Problem formulation

We model the input US in-phase and quadrature (IQ) signal **S** as a linear combination of three components: the tissue (or clutter) signal **T**, the super-resolved MB signal **x** observed through the system model **DH**, and additive noise **N**:

$$\mathbf{S} = \mathbf{T} + \mathbf{DHx} + \mathbf{N}, \tag{1}$$

In this formulation, $\mathbf{H} \in \mathbb{R}^{N_h \times N_h}$ represents the PSF, which is assumed to be Block Circulant with Circulant Blocks (BCCB) matrice. $\mathbf{D} \in \mathbb{R}^{N_l \times N_h}$ is a spatial decimation (downsampling) operator, and **x** denotes the super-resolved MB signal to be estimated. Also, N_h and N_l denote the dimensions of the super-resolved and original spatial grids, respectively, with $N_h = d \times N_l$ and $d = dx \times dz$, with d_z and d_x representing the resolution scaling factors in the axial (z) and lateral (x) directions.

In US imaging, tissue signals typically exhibit strong spatiotemporal coherence, often exceeding that of slowly moving MBs, which facilitates their effective separation [8]. Based on this observation, we model **T** as a low-rank component and **x** as sparse. The goal of this work is to recover a clean, noise-free, tissue-suppressed, and super-resolved estimate of **x** from the corrupted measurements **S**. This leads to the following optimization problem:

$$[\hat{\mathbf{x}}, \hat{\mathbf{T}}] = \arg\min_{\mathbf{x},\mathbf{T}} \|\mathbf{S} - \mathbf{DHx} - \mathbf{T}\|_F^2 + \epsilon\|\mathbf{x}\|1 + \beta\|\mathbf{T}\|* \tag{2}$$

It is worth noting that Equation (2) represents a more generalized form of the conventional Robust Principal Component Analysis (RPCA) optimization problem [12], [13], [17]. However, classical RPCA solutions are not directly applicable, necessitating the development of more sophisticated algorithms, which are introduced in the following subsection.

B. Our proposed method: SMOS

A practical strategy to optimize Equation (2) involves introducing an auxiliary variable to enable the decomposition of the problem into three subproblems, as done in the RPCA framework [13], [18]. These subproblems align with the data fidelity term and the regularization terms promoting sparsity and low-rank structure, forming a three-block convex optimization framework. Although the Alternating Direction Method of Multipliers (ADMM) is well-suited for such formulations, its theoretical convergence guarantees hold only for two-block structures. In three-block settings, convergence is not generally assured unless certain stringent conditions are satisfied [19]. Keeping this in mind, we reformulate Equation (2) as a two-block problem by expressing it as a regularized least-squares objective and employing proximal operators for the regularization components. Specifically, we introduce two auxiliary variables, **V** and **K**, with an additional composite variable, resulting in the following formulations:

$$\begin{aligned}
\mathbf{P}_1 &= [\mathbf{DH} \quad \mathbf{I}_{N_h}];\ \mathbf{P}_2 = [\mathbf{I}_{N_h} \quad \mathbf{0}];\ \mathbf{P}_3 = [\mathbf{0} \quad \mathbf{I}_{N_h}],\\
\tilde{\mathbf{x}} &= [\mathbf{x} \quad \mathbf{K}]^T; \tilde{\mathbf{V}} = [\mathbf{V} \quad \mathbf{T}]^T,\\
f(\tilde{\mathbf{x}}) &= \frac{1}{2}\|\mathbf{S} - \mathbf{P}_1\tilde{\mathbf{x}}\|_F^2,\\
g(\tilde{\mathbf{V}}) &= \epsilon\left\|\mathbf{P}_2\tilde{\mathbf{V}}\right\|_1 + \tau\left\|\mathbf{P}_3\tilde{\mathbf{V}}\right\|_*,
\end{aligned} \tag{3}$$

where $\mathbf{I}_{N_h}$ denotes an identity matrix that has the same dimension as **DH**. With these definitions, our optimization problem (2) has the form:

$$\arg\min_{\tilde{\mathbf{x}},\tilde{\mathbf{V}}} f(\tilde{\mathbf{x}}) + g(\tilde{\mathbf{V}}) \quad \text{subject to } \tilde{\mathbf{x}} = \tilde{\mathbf{V}}, \tag{4}$$

and thereby yields an augmented Lagrangian expression:

$$L(\tilde{\mathbf{x}}, \tilde{\mathbf{V}}, \boldsymbol{\delta}) = f(\tilde{\mathbf{x}}) + g(\tilde{\mathbf{V}}) + \frac{\tau}{2}\left\|\tilde{\mathbf{x}} - \tilde{\mathbf{V}} + \frac{\boldsymbol{\delta}}{\tau}\right\|_2^2 - \frac{1}{2\tau}\|\boldsymbol{\delta}\|_2^2 \tag{5}$$

By applying ADMM, solving Equation (2) can be approached by iteratively addressing the following subproblems:

$$\tilde{\mathbf{x}}^{k+1} = \arg\min_{\tilde{\mathbf{x}}} f(\tilde{\mathbf{x}}) + \frac{\tau}{2}\left\|\tilde{\mathbf{x}} - \tilde{\mathbf{V}}^{k+1} + \frac{\boldsymbol{\delta}^k}{\tau}\right\|_2^2 \tag{6}$$

$$\tilde{\mathbf{V}}^{k+1} = \arg\min_{\tilde{\mathbf{V}}} g(\tilde{\mathbf{V}}) + \frac{\tau}{2}\left\|\tilde{\mathbf{x}}^k - \tilde{\mathbf{V}} + \frac{\boldsymbol{\delta}^k}{\tau}\right\|_2^2 \tag{7}$$

$$\boldsymbol{\delta}^{k+1} = \boldsymbol{\delta}^k + \tau\left(\tilde{\mathbf{x}}^{k+1} - \tilde{\mathbf{V}}^{k+1}\right) \tag{8}$$

Using the definitions in (3), the resolution of each step is:

$$\mathbf{K}^{k+1} = \arg\min_{\mathbf{K}} \frac{1}{2}\left\|\mathbf{S} - \mathbf{DHx}^k - \mathbf{K}\right\|_F^2 + \frac{\tau}{2}\left\|\mathbf{K} - \mathbf{T}^k + \frac{\boldsymbol{\delta}_2^k}{\tau}\right\|_2^2 \tag{9}$$

$$\mathbf{x}^{k+1} = \arg\min_{\mathbf{x}} \frac{1}{2}\left\|\mathbf{S} - \mathbf{DHx} - \mathbf{K}^{k+1}\right\|_F^2 + \frac{\tau}{2}\left\|\mathbf{x} - \mathbf{V}^k + \frac{\boldsymbol{\delta}_1^k}{\tau}\right\|_2^2 \tag{10}$$

$$\mathbf{T}^{k+1} = \arg\min_{\mathbf{T}} \beta\|\mathbf{T}\|_* + \frac{\tau}{2}\left\|\mathbf{K}^{k+1} - \mathbf{T} + \frac{\boldsymbol{\delta}_2^k}{\tau}\right\|_2^2 \tag{11}$$

$$\mathbf{V}^{k+1} = \arg\min_{\mathbf{V}} \epsilon\|\mathbf{V}\|_1 + \frac{\tau}{2}\left\|\mathbf{x}^{k+1} - \mathbf{V} + \frac{\boldsymbol{\delta}_1^k}{\tau}\right\|_2^2 \tag{12}$$

$$\boldsymbol{\delta}_2^{k+1} = \boldsymbol{\delta}_2^k + \tau\left(\mathbf{K}^{k+1} - \mathbf{T}^{k+1}\right) \tag{13}$$

$$\boldsymbol{\delta}_1^{k+1} = \boldsymbol{\delta}_1^k + \tau\left(\mathbf{x}^{k+1} - \mathbf{V}^{k+1}\right) \tag{14}$$

These six steps in Equations (9)–(14) constitute the overall framework of our solution. Since the final two steps involve only parameter updates, we focus our discussion below on the remaining steps. Also, it is worth noting that these six steps admit closed-form solutions. However, obtaining a closed-form solution for (10) is particularly challenging, as it involves solving an ℓ_2–ℓ_2 single-image super-resolution problem.

1) Step 1: To solve Equation (9), we take its derivative with respect to **K**, set it equal to zero, and solve for $\mathbf{K}^{k+1}$. This yields:

$$\mathbf{K}^{k+1} = \frac{1}{1+\tau}(\mathbf{S} - \mathbf{DH}\,\mathbf{x}^k + \tau\mathbf{T}^k - \boldsymbol{\delta}_2^k) \tag{15}$$

2) Step 2: As previously noted, solving the optimization problem formulated in Equation (10) presents greater complexity demands compared to the other steps. The main goal in this step is to reconstruct a high-resolution image, denoted by **x**, from its blurred, downsampled, and noisy observation $\mathbf{K}^{k+1}$. This reconstruction is regularized by the prior term

$\left|\mathbf{x}-\left(\mathbf{V}^k-\frac{\boldsymbol{\delta}_1^k}{\tau}\right)\right|_2$, which incorporates information from earlier iterations to regularize the solution.

First, by introducing the notations $\mathbf{K}=\mathbf{S}-\mathbf{K}^{k+1}$, $\tau=\tau/2$, and $\overline{\mathbf{x}}=\mathbf{V}^k-\frac{1}{\tau}\boldsymbol{\delta}_1^k$, Equation (10) can be equivalently expressed as the following simplified optimization problem:

$$\mathbf{x}^{k+1}=\arg\min_{\mathbf{x}}\left(\frac{1}{2}||\mathbf{K}-\mathbf{DHx}||_F^2+\tau||\mathbf{x}-\overline{\mathbf{x}}||_F^2\right), \quad (16)$$

The solution to the problem (16) can be found in [20], to which the reader is referred for further details. For the sake of completeness, however, we briefly outline the main steps with some adaptations relevant to our current problem. Specially, since $\mathbf{H}$ is BCCB, it can be diagonalized in the Fourier domain, leading to the following expression:

$$\mathbf{H}=\mathbf{F}^H\boldsymbol{\Lambda}\mathbf{F} \quad \text{and its conjugate transpose} \quad \mathbf{H}^H=\mathbf{F}^H\boldsymbol{\Lambda}^H\mathbf{F},$$

where $\boldsymbol{\Lambda}\in\mathbb{C}^{N_h\times N_h}$ is a diagonal matrix containing the 2D Fourier transform of the zero-padded PSF, and $\mathbf{F}\in\mathbb{C}^{N_h\times N_h}$ is the unitary 2D Fourier transform matrix satisfying $\mathbf{F}^H=\mathbf{F}^{-1}$. Following [20], the decimation operator $\mathbf{D}$ and its conjugate transpose are assumed to perform zero-insertion interpolation, which implies $\mathbf{DD}^H=\mathbf{I}_{N_l}$. We also denote $\underline{\mathbf{D}}\triangleq\mathbf{D}^H\mathbf{D}$ for convenience.

Thus, the closed-form solution for (16) is given by:

$$\mathbf{x}^{k+1}=\left(\mathbf{H}^H\underline{\mathbf{D}}\mathbf{H}+2\tau\mathbf{I}_{N_h}\right)^{-1}\left(\mathbf{H}^H\mathbf{D}^H\mathbf{K}+2\tau\overline{\mathbf{x}}\right), \quad (17)$$

or, in the Fourier domain, using (I), it becomes:

$$\mathbf{x}^{k+1}=\mathbf{F}^H\left(\boldsymbol{\Lambda}^H\mathbf{F}\underline{\mathbf{D}}\mathbf{F}^H\boldsymbol{\Lambda}+2\tau\mathbf{I}_{N_h}\right)^{-1}\mathbf{Fk}, \quad (18)$$

where $\mathbf{k}=\left(\mathbf{F}^H\boldsymbol{\Lambda}^H\mathbf{F}\mathbf{D}^H\mathbf{K}+2\tau\overline{\mathbf{x}}\right)$.

However, these analytical solutions in Equations (17) and (18) are not tractable in practice. Specifically, in (17), the involved matrices are extremely large with dimensions $N_h\times N_h$, making direct inversion computationally prohibitive. Although in (18) the multiplications involving $\boldsymbol{\Lambda}$ reduce to simple element-wise operations, the term involving $\mathbf{D}$ remains complex and difficult to handle due to its non-diagonal structure.

To overcome these limitations and efficiently compute the analytical solution in (18), $\mathbf{F}\underline{\mathbf{D}}\mathbf{F}^H$ can be expressed as :

$$\mathbf{F}\underline{\mathbf{D}}\mathbf{F}^H=(\mathbf{I}_{N_t})\otimes\frac{1}{dr}\left(\mathbf{J}_{dr}\otimes\mathbf{I}_{N_zN_x}\right), \quad (19)$$

where $dr=dzdx$, $\mathbf{I}_v\in\mathbb{R}^{v\times v}$ is the $v\times v$ identity matrix, and $\otimes$ denotes the Kronecker product. Using this property, (18) can be reformulated as:

$$\mathbf{x}^{k+1}=\mathbf{F}^H\left(\frac{1}{dr}\underline{\boldsymbol{\Lambda}}^H\underline{\boldsymbol{\Lambda}}+2\tau\mathbf{I}_{N_h}\right)^{-1}\mathbf{Fk}, \quad (20)$$

where $\underline{\boldsymbol{\Lambda}}\in\mathbb{C}^{N_l\times N_h}$ is defined as:

$$\underline{\boldsymbol{\Lambda}}=\left[(\mathbf{I}_{N_t})\otimes\left(\mathbf{1}_{dr}^T\otimes\mathbf{I}_{N_zN_x}\right)\right]\boldsymbol{\Lambda}.$$

This reformulation (20) significantly simplifies the problem and permits further optimization by applying the matrix inversion lemma [21]:

$$\mathbf{x}^{k+1}=\frac{1}{2\tau}\mathbf{k}-\frac{1}{2\tau}\mathbf{F}^H\underline{\boldsymbol{\Lambda}}^H\left(2\tau dr\mathbf{I}_{N_l}+\underline{\boldsymbol{\Lambda}}\underline{\boldsymbol{\Lambda}}^H\right)^{-1}\underline{\boldsymbol{\Lambda}}\mathbf{Fk}. \quad (21)$$

Finally, by substituting $\mathbf{K}=\mathbf{S}-\mathbf{K}^{k+1}$, $\tau=\frac{\tau}{2}$, and $\overline{\mathbf{x}}=\mathbf{V}^k-\frac{1}{\tau}\boldsymbol{\delta}_1^k$ into (21), we obtain:

$$\mathbf{x}^{k+1}=\mathbf{k}-\mathbf{F}^H\underline{\boldsymbol{\Lambda}}^H\left(dr\mathbf{I}_{N_l}+\underline{\boldsymbol{\Lambda}}\underline{\boldsymbol{\Lambda}}^H\right)^{-1}\underline{\boldsymbol{\Lambda}}\mathbf{Fk}. \quad (22)$$

where $\mathbf{k}=\mathbf{F}^H\boldsymbol{\Lambda}^H\mathbf{F}\mathbf{D}^H\left(\mathbf{S}-\mathbf{K}^{k+1}\right)+\tau\left(\mathbf{V}^k-\frac{1}{\tau}\boldsymbol{\delta}_1^k\right)$.

Importantly, the numerical implementation of (21) requires only one fast Fourier transform (FFT) and one inverse FFT, in addition to element-wise multiplications. This yields a substantial reduction in computational cost compared to the original formulation in (17), decreasing complexity from $\mathcal{O}(N_h^3)$ to $\mathcal{O}(N_h\log N_h)$, allowing an efficient implementation.

3) Step 3 and 4: To solve (11), (12), we employed Singular value thresholding [22] and Soft thresholding techniques [23]. These lead to:

$$\begin{aligned}\mathbf{T}^{k+1}&=\arg\min_{\mathbf{T}}\beta\left\|\mathbf{T}\right\|_*+\frac{\tau}{2}\left\|\mathbf{T}-(\mathbf{K}^{k+1}+\frac{1}{\tau}\boldsymbol{\delta}_2^k)\right\|_2^2\\&=\mathbf{USoft}_{\frac{\beta}{\tau}}[\triangle]\mathbf{V}^T \quad \text{with } \mathbf{U}\triangle\mathbf{V}^T=\mathbf{K}^{k+1}+\frac{1}{\tau}\boldsymbol{\delta}_2^k \quad (23)\end{aligned}$$

where $\mathbf{Soft}_\tau[\cdot]$ denotes the soft-thresholding operator with parameter τ applied to the singular values. And:

$$\begin{aligned}\mathbf{V}^{k+1}&=\arg\min_{\mathbf{V}}\epsilon\left\|\mathbf{V}\right\|_1+\frac{\tau}{2}\left\|\mathbf{V}-(\mathbf{x}^{k+1}+\frac{1}{\tau}\boldsymbol{\delta}_1^k)\right\|_2^2\\&=\mathbf{Soft}_{\frac{\epsilon}{\tau}}[\mathbf{x}^{k+1}+\frac{1}{\tau}\boldsymbol{\delta}_1^k] \quad (24)\end{aligned}$$

Finally, considering all the steps outlined above, the complete pseudo-code for the proposed SMOS algorithm is presented in Algorithm 1.

Algorithm 1: Pseudo algorithm of SMOS

Initialize: $\mathbf{x}$, $\mathbf{V}$, $\mathbf{K}$, $\mathbf{T}$, $\boldsymbol{\delta}_1$, $\boldsymbol{\delta}_2$.
While not convergent do:
Step 1: $\mathbf{K}^{k+1}=\frac{1}{1+\tau}\left(\mathbf{S}-\mathbf{DHx}^k+\tau\mathbf{T}^k-\boldsymbol{\delta}_2^k\right)$.
Step 2: $\mathbf{x}^{k+1}=\mathbf{k}-\mathbf{F}^H\underline{\boldsymbol{\Lambda}}^H\left(dr\mathbf{I}_{N_l}+\underline{\boldsymbol{\Lambda}}\underline{\boldsymbol{\Lambda}}^H\right)^{-1}\underline{\boldsymbol{\Lambda}}\mathbf{Fk}$,
where $\mathbf{k}=\mathbf{F}^H\boldsymbol{\Lambda}^H\mathbf{F}\mathbf{D}^H\left(\mathbf{S}-\mathbf{K}^{k+1}\right)+\tau\left(\mathbf{V}^k-\frac{1}{\tau}\boldsymbol{\delta}_1^k\right)$.
Step 3: $\mathbf{T}^{k+1}=\mathbf{USoft}_{\frac{\beta}{\tau}}[\triangle]\mathbf{V}^T$,
with $\mathbf{U}\triangle\mathbf{V}^T=SVD(\mathbf{K}^{k+1}+\frac{1}{\tau}\boldsymbol{\delta}_2^k,r_f)$.
Step 4: $\mathbf{V}^{k+1}=\mathbf{Soft}_{\frac{\epsilon}{\tau}}\left[\mathbf{x}^{k+1}+\frac{1}{\tau}\boldsymbol{\delta}_1^k\right]$.
Step 5: $\boldsymbol{\delta}_2^{k+1}=\boldsymbol{\delta}_2^k+\tau\left(\mathbf{K}^{k+1}-\mathbf{T}^{k+1}\right)$.
Step 6: $\boldsymbol{\delta}_1^{k+1}=\boldsymbol{\delta}_1^k+\tau\left(\mathbf{x}^{k+1}-\mathbf{V}^{k+1}\right)$.

III. Experimental results and discussions

In this section, we first introduce the datasets and metrics utilized in our study. We then provide both qualitative and quantitative comparisons between our proposed method SMOS and several established, SOTA benchmarks, including RS-ULM [5], NP-ULM [6], SRPCA [12][2]. Finally, we present the

[2]In this study, we focused exclusively on model-based methods and exclude deep learning (DL) techniques for two primary reasons. First, most DL techniques are typically trained on synthetic datasets and subsequently applied to *in vivo* data for inference, a pipeline that is fundamentally incompatible with iterative model-based methods. Second, the methodologies behind many DL approaches are not fully disclosed by their authors, making a fair and rigorous comparison infeasible.

computational complexities of the studied methods, followed by a discussion to further analyze the key characteristics of the proposed algorithm.

A. Datasets and Metrics

We begin by evaluating all methods on an enhanced *in silico* dataset, adapted from the original synthetic dataset introduced in [5]. The original dataset included only MBs without tissue patterns and contained low MB concentrations - conditions that do not accurately represent real-world scenarios. To address this, we developed an improved version of the original dataset to better simulate practical imaging conditions:

- First, we increased the MB concentration by summing groups of four blocks, thereby allowing more MBs to appear per frame. Each group was composed of blocks sampled at uniform intervals (e.g., blocks 1, 6, 11, and 16 for the first group).
- Next, we projected the MB locations onto a super-resolved grid at 10× the original spatial resolution to generate the ground truth (GT) target. This target was then convolved with a PSF and downsampled 10 times.
- Finally, we introduced tissue patterns and added white Gaussian noise to generate the final input observations.

For the *in silico* benchmarking, we utilized several full-reference image quality metrics, as used in previous studies [5], [18], including Jaccard Accuracy (%), Lateral Error, Axial Error, Structure Similarity Index Measure (SSIM), and Normalized Root Mean Square Error (nRMSE).

We also evaluated all methods on two *in vivo* datasets.

- The first dataset, named the WKY dataset [12], features brain angiographies from 200 grams rat using Doppler contrast-enhanced US, with bolus injections at regular intervals. It was acquired at UMR 1253, iBrain, Universite de Tours, France with approval from the university's regulatory authorities. It includes 40,000 frames across 80 blocks.
- The second dataset was adopted from the supplementary materials of [5]. It includes in total 200,000 US frames of a 260g male Sprague-Dawley rat brain acquired post-craniotomy at 1kHz using a 15 MHz linear probe. MB injections were administered at 2×10^8 MBs/mL, and imaging was conducted with a Vantage 256 scanner.

For the *in vivo* benchmarking, we assessed image quality using several metrics commonly employed in *in vivo* studies, including Contrast Ratio (CR) [18], Contrast-to-Noise Ratio (CNR) [24], and Saturation [5].

B. Practical implementation details

First, from an implementation standpoint, prior research [18] has highlighted the high computational burden of solving Equation (11), primarily due to the need for computing a full SVD on large matrices. To alleviate this burden, we adopt a strategy inspired by [18], substituting the full SVD with a truncated version that retains only the leading r_f components.

Second, to ease the deployment, SMOS features a simple tuning strategy in which ϵ is empirically adjusted to achieve optimal sparsity, while β and τ are kept fixed across all experiments. This results in a tuning complexity comparable to that of RS-ULM [5] and NP-ULM [6], and substantially simpler than the configuration required for SRPCA [12].

Third, in the *in vivo* experiments, our proposed approach is compatible with both automatic and manually extracted PSF estimation techniques. For the WKY dataset, we utilized the automatic PSF estimation technique approach outlined in Michailovich et *al.* [25]. In contrast, for the PALA rat brain dataset, the PSF was manually extracted by empirically selecting a MB from a filtered frame, following the procedure outlined in [12]. This intentional variation was to assess the robustness of our approach under differing conditions. Further details are provided in the Discussion section III-F.

Finally, in the subsequent subsections, the *in silico* experiment results for all evaluated methods are reported at a super-resolution factor of 10×, while the *in vivo* results are presented at both 4× and 10× magnification levels. All experiments were conducted on a workstation equipped with an Intel(R) Xeon(R) W-1290 CPU and 128GB of RAM.

C. In silico results

Figure 2 presents the qualitative results of all methods evaluated on the enhanced *in silico* dataset. A visual assessment of these results reveals that our proposed method, SMOS, consistently delivers the highest-quality reconstructions, with SRPCA ranking as the second-best performer. In contrast, RS-ULM and NP-ULM yield the poorest results, exhibiting similar levels of reconstruction quality. Particularly, SMOS excels at reconstructing primary structures, effectively preserving both fine details and overall data fidelity. This advantage is particularly evident in the horizontal curved structures and vertical tubes, where other methods - including SRPCA - either lose minor details or experience significant structural degradation as observed in RS-ULM and NP-ULM.

TABLE II: Quantitative metrics on the *in silico* dataset. **Bold** numbers indicate better performance.

Metrics	RS-ULM	NP-ULM	SRPCA	SMOS
Jaccard Accuracy (%) ↑	4.82	4.60	17.63	**20.40**
SSIM (%) ↑	0.894	0.895	0.898	**0.903**
Lateral Error ↓	0.22	0.24	0.17	**0.16**
Axial Error ↓	0.16	0.16	0.17	0.16
NRMSE ↓	0.058	0.059	0.060	**0.056**

We also present the corresponding quantitative results in Table II, which further support previous qualitative findings. Specifically, SMOS achieves the highest SSIM, reflecting its strong capability to preserve overall structures. Moreover, it attains the highest precision and the lowest noise levels in challenging areas such as the "ULM" text and the four piles in the right corner. Other performance metrics also confirmed that our method outperforms the alternatives.

We argue that our method's overperformance is driven by these primary factors. First, unlike RS-ULM and NP-ULM, our approach explicitly accounts for the impact of PSF, which substantially enhances reconstruction. Second, compared to SRPCA whose sequential processing can accumulate errors across stages and lead to suboptimal results, our method benefits from a more integrated framework.

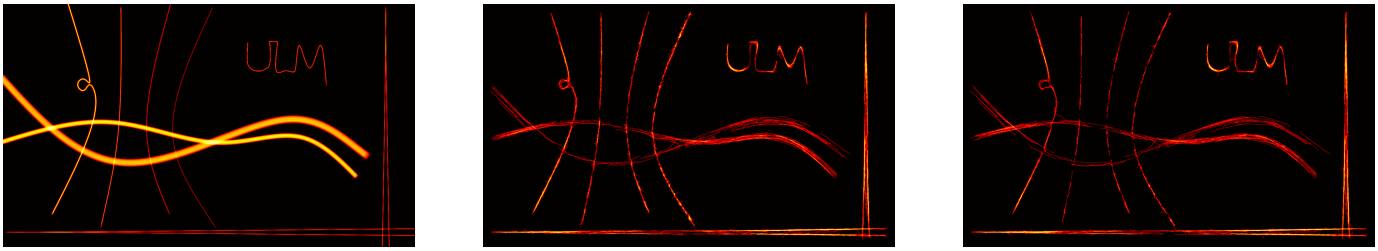

(a) Ground Truth (GT) (b) RS-ULM (c) NP-ULM

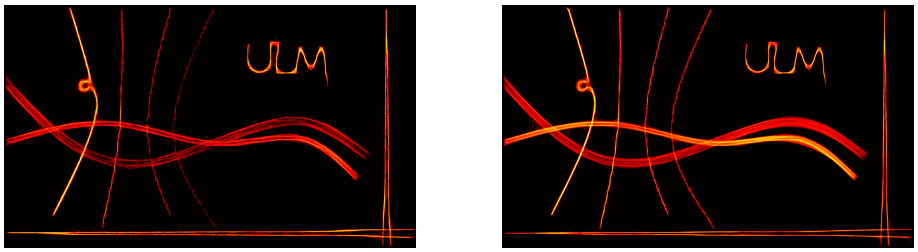

(d) SRPCA (e) SMOS

Fig. 2: Rendering results of all studied methods on the *in silico* dataset. Each subfigure shows output from a specific method.

D. In vivo results

1) Results on the WKY dataset: Figure 3 illustrates the performance of each benchmark method on the WKY dataset at a SR factor of 4× (SR=4), while Figure 4 displays the corresponding results at SR=10.

A deep glance on the visualized results at SR=4 reveals that SMOS consistently outperforms existing techniques in reconstructing microvascular structures, particularly in capturing fine anatomical details. For instance, in Region 3 of Figure 3, RS-ULM fails to recover the morphology of small vessels, while SRPCA and NP-ULM show moderate improvements - albeit with notable limitations. NP-ULM introduces significant artifact. Although SRPCA achieves performance closer to SMOS, its reconstruction still exhibits discontinuities, missing vessel segments in Region 3, and artifacts aligned parallel to major vessels in Region 2. At SR=10 (Figure 4), SMOS and SRPCA show comparable overall performance, however, important differences remain. For example, in Region 4, SRPCA introduces structural artifacts aligned with primary vessels, and in Region 3, it is less effective than SMOS in preserving vessel morphology. Finally, it can be seen that SMOS and SRPCA outperform RS-ULM and NP-ULM.

Metrics	RS-ULM	NP-ULM	SRPCA	SMOS
Saturation (%)↑	29.35	**42.87**	30.90	38.43
CR (dB) ↑	18.08	16.01	21.35	**22.80**
CNR (dB) ↑	19.22	19.11	18.50	**19.76**

TABLE III: Quantitative metrics on WKY dataset at SR=4.

Metrics	RS-ULM	NP-ULM	SRPCA	SMOS
Saturation (%) ↑	19.89	27.48	26.85	**30.14**
CR (dB) ↑	17.12	19.10	21.46	**25.31**
CNR (dB) ↑	15.42	13.83	16.05	**20.07**

TABLE IV: Quantitative metrics on WKY dataset at SR=10.

These observations are consistent with quantitative assessments, summarized in Tables III (SR=4) and IV (SR=10), respectively. It is significant to mention that among the evaluation metrics, saturation is commonly used to assess the ability to detect new structures [5]. However, as highlighted in prior studies [6], saturation is also known to be highly sensitive to noise. To provide a more comprehensive evaluation of structural recovery, we considered both saturation and CNR.

In Table IV, SMOS achieves the highest scores across all metrics: saturation, CR, and CNR. In Table III, SMOS ranks first in CR and CNR, and ranks second in saturation, with NP-ULM reporting the highest saturation. However, we contend that NP-ULM's elevated saturation score is primarily driven by noise-induced artifacts rather than true structural recovery. This is supported by its significantly lower CNR relative to both SRPCA and SMOS, indicating that the apparent increase in saturation is achieved at the expense of image quality and structural fidelity. Therefore, when evaluating structural recovery based on both saturation and CNR, SMOS demonstrates the most consistent and reliable performance across both SR=4 and SR=10.

In terms of contrast, SMOS and SRPCA emerge as the top performers, with SMOS consistently surpasses all other methods. At both SR=4 and SR=10, our method achieves the highest quantitative values for both CR and CNR, indicating SMOS's superior contrast preservation with less noise.

2) Results on the PALA dataset: The rendering results of all methods in the PALA dataset at both SR=4 and SR=10 are shown in Figures 5 and 6, respectively.

At SR=4, RS-ULM and NP-ULM generally produce blurred, poorly defined, and hazy reconstructions, particularly in localized areas such as Regions 1 and 2 of Figure 5. In contrast, SRPCA and SMOS demonstrate markedly improved performance, yielding clearer and more coherent structures. However, even in these regions, SRPCA still exhibits disconnected pixels in structures, while SMOS successfully reconstructs fine-grained and continuous vessel structures. At SR=10, both SMOS and SRPCA continue to lead in performance, though

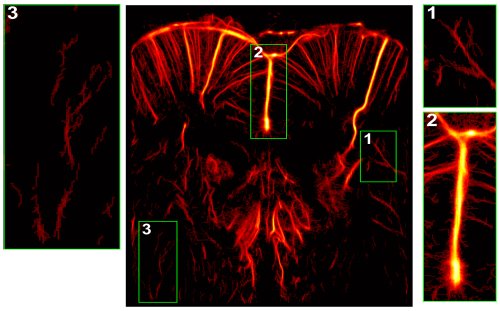

(a) RS-ULM

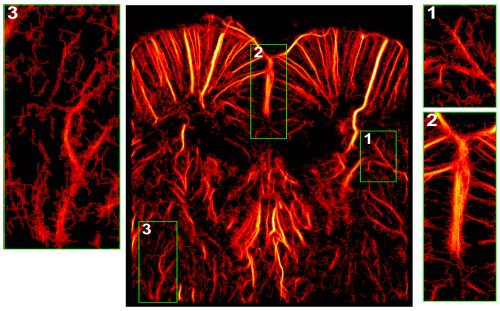

(b) NP-ULM

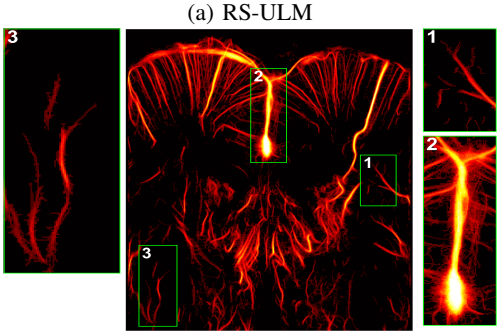

(c) SRPCA

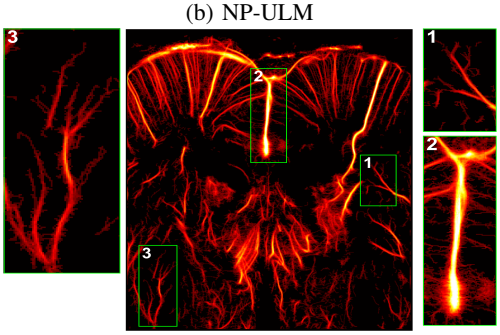

(d) SMOS

Fig. 3: Rendering results of all studied methods on the WKY dataset at SR=4. A zoom-in on the regions highlighted by the blue rectangles reveals notable differences in reconstruction among the methods.

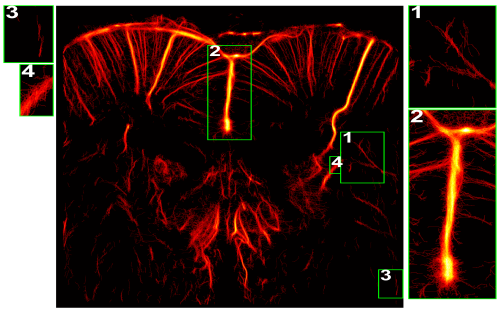

(a) RS-ULM

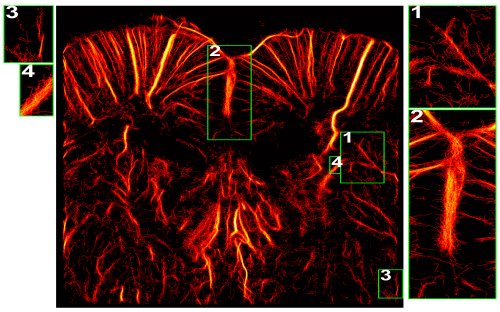

(b) NP-ULM

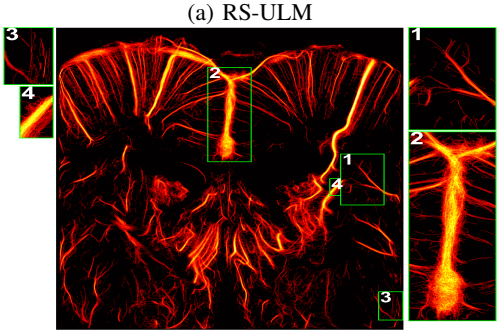

(c) SRPCA

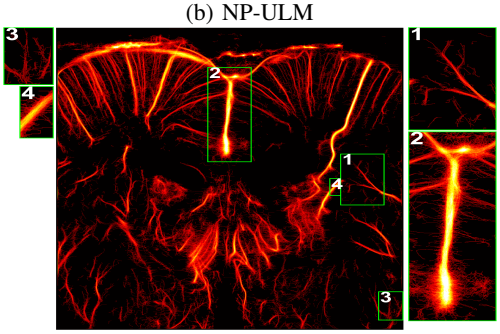

(d) SMOS

Fig. 4: Rendering results of all studied methods on the WKY dataset at SR=10.

SRPCA tends to generate denser, less sparse reconstructions. A more detailed examination, particularly in Region 1 of Figure 6, suggests that our approach more effectively captures fine structural details, such as microvessels. In terms of contrast, both methods consistently outperform RS-ULM and NP-ULM, with our method achieving the highest overall contrast across both SR levels. Notably, SMOS enhances contrast especially in dominant anatomical structures - for instance, Region 3 of Figures 5 and 6 - as well as in several other key areas.

These findings align with the qualitative metrics presented in Tables V and VI. At SR=4, our method consistently outperforms SRPCA in both saturation and CR. While SRPCA achieves slightly higher saturation at SR=10, our approach still leads in CR. The tables also reveal that although RS-

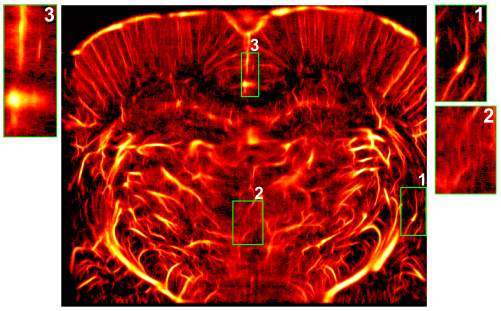

(a) RS-ULM

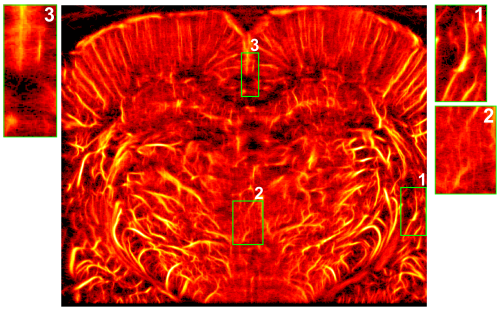

(b) NP-ULM

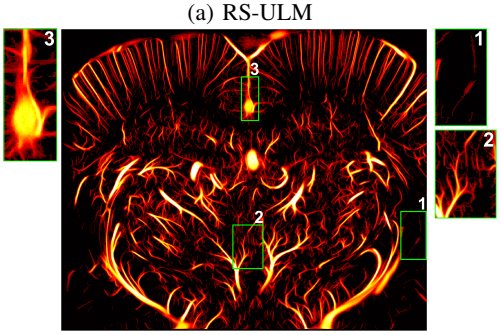

(c) SRPCA

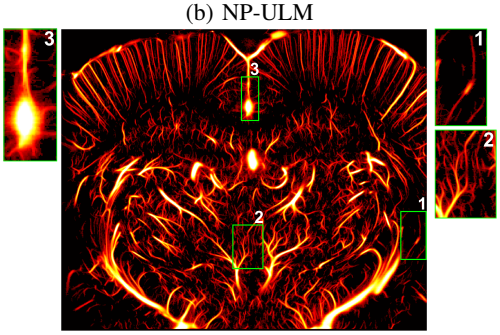

(d) SMOS

Fig. 5: Rendering results of all studied methods on the PALA dataset [5] at SR=4.

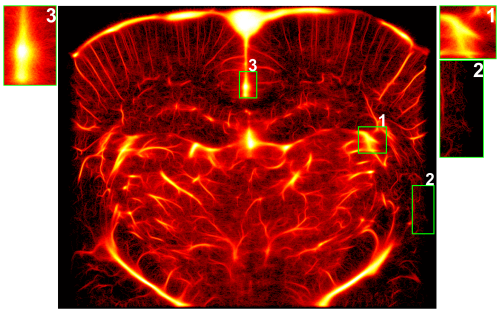

(a) RS-ULM

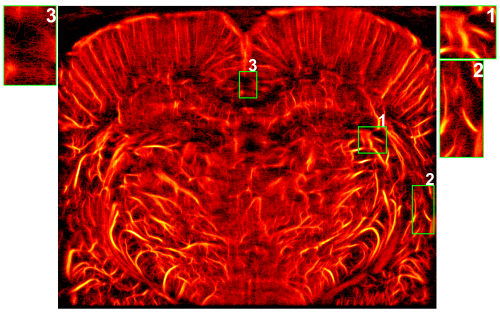

(b) NP-ULM

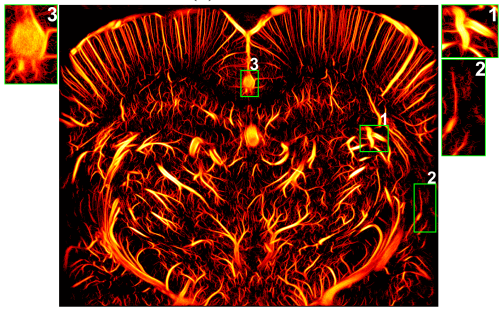

(c) SRPCA

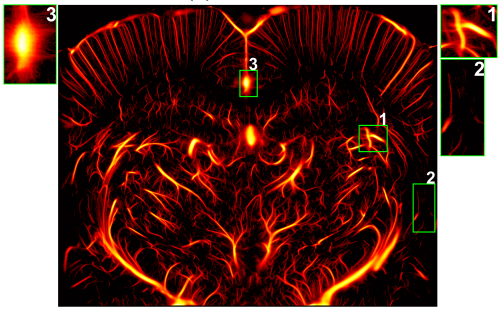

(d) SMOS

Fig. 6: Rendering results of all studied methods on the PALA dataset at SR=10.

ULM and NP-ULM report high saturation values, their CNR is significantly lower. As previously discussed in the context of the WKY dataset, this elevated saturation is largely driven by noise and the inadequate suppression of clutter, rather than genuine structural recovery.

Indeed, both SMOS and SRPCA substantially outperform RS-ULM and NP-ULM in reconstructing well-defined anatomical structures and microvasculature. For example, NP-ULM fails to recover a critical structure in Region 3 (Figure 6) and introduces multiple artifacts, while RS-ULM misses several vascular structures in Regions 1 and 2.

E. Comparison of Computational Complexities

We provide a comprehensive analysis of computational complexities of all studied methods in Table VII. Specifically:

- In SMOS algorithm, Step 2 is the most computationally intensive, with a per-frame complexity of $\mathcal{O}(N_h \log N_h)$.

Metrics	RS-ULM	NP-ULM	SRPCA	SMOS
Saturation (%) ↑	**80.00**	70.34	36.50	46.13
CR (dB) ↑	26.93	21.19	32.28	**34.45**
CNR (dB) ↑	19.88	21.25	26.18	**28.70**

TABLE V: Quantitative metrics on PALA dataset [5] at SR=4.

Metrics	RS-ULM	NP-ULM	SRPCA	SMOS
Saturation (%) ↑	86.57	78.27	47.59	43.42
CR (dB) ↑	22.44	21.38	30.19	**32.51**
CNR (dB) ↑	19.98	18.02	22.67	**24.55**

TABLE VI: Quantitative metrics on PALA dataset at SR=10.

Method	Total complexity	Time (s) ↓
RS-ULM	$\mathcal{O}([\alpha+1]\cdot m\cdot n^2)$	0.35
NP-ULM	$\mathcal{O}([\alpha+2]\cdot m\cdot n^2)$	0.62
SRPCA	$\mathcal{O}(N_{iter}\cdot R_f^2\cdot m^2\cdot n^2)$	92.54
Ours	$\mathcal{O}(\eta\cdot N_{iter}\cdot R_f^2\cdot m^2\cdot n\cdot\log(m^2\cdot R_f^2))$	12.95

TABLE VII: A summary of the computational complexity of all algorithms, along with their running times for a sample block of the PALA dataset. The values of α and η are empirically determined to be 0.5 and 4, respectively.

Let denote R_f the SR factor, n the number of temporal frames, and m the first dimension of the Casorati matrix. Therefore, the theoretical complexity for processing a single data block is $\mathcal{O}(N_{\text{iter}}\cdot n\cdot m^2\cdot R_f^2\cdot\log(m^2\cdot R_f^2))$. Empirically, we observe that the actual implementation incurs approximately a η-fold overhead compared to the theoretical estimation, where $\eta\approx 4$.

- For NP-ULM, they adopted the same pipeline as RS-ULM, with the only difference lying in the MB detection. This step requires iterating through the Casorati matrix and estimating the temporal median value at each pixel, resulting in a computational complexity of $\mathcal{O}(m\cdot n^2)$. Their overall complexity is thus $\mathcal{O}([\alpha+2]\cdot m\cdot n^2)$.
- For comparison, the computational complexities of RS-ULM and SRPCA are obtained from [12].

Table VII also presents the actual runtime of each algorithm on a sample block comprising 100 frames from the PALA dataset. With $N_{\text{iter}}=20$ and $R_f=4$, our method SMOS is theoretically about 15 times faster than SRPCA. In contrast, RS-ULM and NP-ULM are approximately 14 and 9 times faster than SMOS, respectively. These theoretical estimates are consistent with empirical runtimes: SMOS runs roughly 7 times faster than SRPCA, though it remains slower than both RS-ULM and NP-ULM.

F. Discussions

As evidenced by the preceding results, our proposed method, SMOS, consistently outperforms both RS-ULM and NP-ULM in terms of reconstruction accuracy, the preservation of fine structural microvessels, and across various quantitative evaluation metrics.

Compared to SRPCA, SMOS exhibits competitive performance while providing several notable advantages and, in certain scenarios, surpasses it. Precisely:

- At SR=4, SMOS outperforms SRPCA across all datasets and all quantitative metrics. Besides better CR, we also achieve higher saturation and CNR than SRPCA, which are clinically meaningful enhancements. Improved saturation, in particular, contributes to more accurate and reliable detection of vascular structures, as noted in [5].
- A further notable advantage of SMOS over SRPCA is its consistently higher contrast in prominent vascular structures and in overall image across all settings.
- The only exception occurs on the PALA dataset at SR=10, where SRPCA yields slightly higher saturation. However, this comes at the expense of reduced CNR and CR, highlighting a trade-off in SRPCA's performance. Moreover, at SR=4 on this dataset, SMOS continues to surpass SRPCA in all metrics.
- Importantly, SMOS also demonstrates strong robustness to variations in PSF estimation techniques, thus mitigating sensitivity to PSF estimation. As illustrated in Figure 7, the results obtained utilizing the manual PSF extraction method closely resemble those shown in Figure 6d using the automated method. In contrast, SRPCA requires a manual PSF extraction, where one must empirically isolate MBs. This procedure is not only labor-intensive but also time-consuming, limiting its practical deployment due to high sensitivity. Therefore, our flexibility not only simplifies the workflow but also enhances practical applicability, making our approach more adaptable and efficient across diverse scenarios.

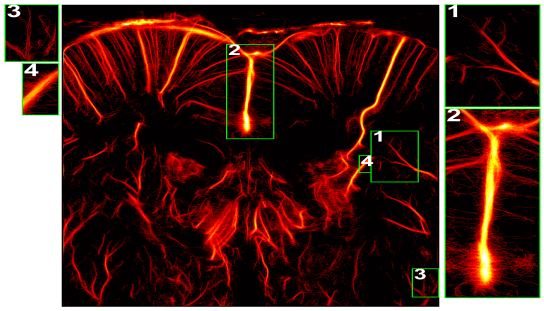

Fig. 7: Rendering results of SMOS on the WKY dataset using manual PSF extraction at SR=10.

We argue that these advantages of our method are not incidental. Figure 8 presents a representative frame from the PALA dataset processed by a traditional SVD-based filter (as used in RS-ULM and NP-ULM), SRPCA, and SMOS. The visualization reveals that both SMOS and SRPCA achieve superior MB separation compared to SVD-based methods, resulting in significantly enhanced reconstructions. Notably, in regions highlighted by green rectangles, SMOS more effectively isolates individual MBs than SRPCAs. This enhanced separation not only improves localization but also supports more continuous and coherent MB tracking, directly contributing to the improved contrast observed in specific regions (e.g., Region 3 in Figures 6 and 5). In other areas, such as the large oblique structure in the lower-right corner, our method produces more spatially well-defined MBs than SRPCA.

Finally, regarding the computational burden, although SMOS operates at a slower speed compared to RS-ULM and NP-ULM, this trade-off is justified by the substantially higher

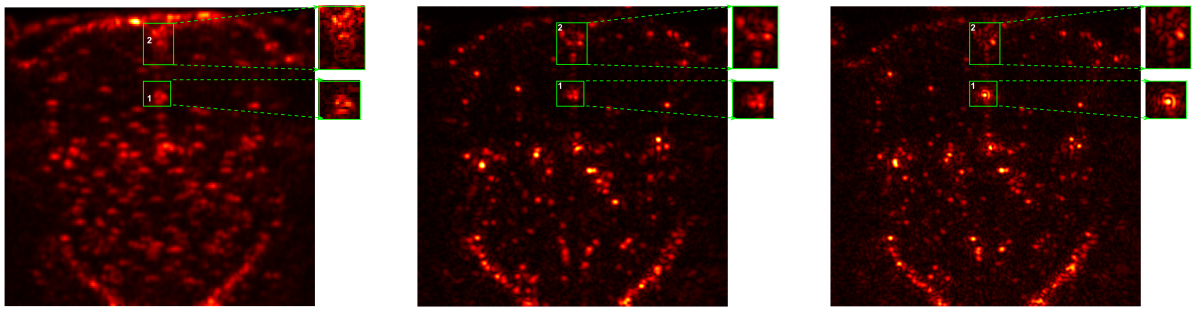

Fig. 8: Visualization of a processed single frame from the PALA dataset. The frame displays results processed by: (a) SVD filtering with a bandpass filter, (b) SMOS, and (c) SRPCA before the localization step.

quality of reconstructions. Notably, our method demonstrates a notable advantage in processing speed - approximately 7 times faster - when compared to the recently introduced SRPCA approach. It is also worth emphasizing that our current implementation has not yet been fully optimized, indicating strong potential for future improvements in efficiency.

IV. Conclusion

In this work, we have introduced SMOS, a model-based framework fo ULM image reconstruction. SMOS is the first approach to jointly address the initial three stages of the conventional ULM pipeline - detection, localization, and accumulation - within a unified optimization framework. Compared to state-of-the-art methods such as RS-ULM and NP-ULM, SMOS demonstrated more robust and accurate reconstructions. In comparison with SRPCA, it delivered comparable performance while offering several notable advantages: enhanced contrast in dominant microvascular vessels, improved performance at SR=4, elimination of exhaustive PSF extraction, and approximately sevenfold reduction in computational cost. For future work, we plan to explore techniques such as deep unfolding on SMOS to enable automatic hyperparameter tuning and PSF estimation, thus increasing the robustness, adaptability, and interpretability of the proposed method.

Acknowledgment

The authors thank Drs. Corentin Alix, Jean-Pierre Remeniéras, and Ayache Bouakaz (INSERM iBrain, Tours, France) for their help in acquiring the *in vivo* WKY dataset.

References

[1] T. Ilovitsh *et al.*, "Acoustical structured illumination for super-resolution ultrasound imaging," *Commun. Biol.*, vol. 1, no. 1, Jan. 2018.

[2] O. Couture *et al.*, "Ultrasound Localization Microscopy and Super-Resolution: A State of the Art," *Ultrafast imaging in biomedical ultrasound*, vol. 65, no. 8, pp. 1304–1320, Aug. 2018.

[3] Christensen-Jeffries *et al.*, "In vivo acoustic super-resolution and super-resolved velocity mapping using microbubbles," *IEEE Trans. Med. Imaging*, vol. 34, no. 2, p. 433–440, Feb. 2015.

[4] S. Dencks *et al.*, "Super-resolution ultrasound: From data acquisition and motion correction to localization, tracking, and evaluation," *IEEE Trans. Ultrason. Ferroelectr. Freq. Control*, vol. 72, no. 4, Apr. 2025.

[5] B. Heiles *et al.*, "Performance benchmarking of microbubble-localization algorithms for ultrasound localization microscopy," *Nat Biomed Eng*, vol. 6, no. 5, p. 605–616, Feb. 2022.

[6] A. Corazza *et al.*, "Microbubble identification based on decision theory for ultrasound localization microscopy," *IEEE Open Journal of Ultrasonics, Ferroelectrics, and Frequency Control*, vol. 3, p. 41–55, 2023.

[7] K. A. Ozgun and B. C. Byram, "Multidimensional clutter filtering of aperture domain data for improved blood flow sensitivity," *IEEE Trans. Ultrason. Ferroelectr. Freq. Control*, vol. 68, no. 8, pp. 2645–2656, 2021.

[8] Y. Desailly *et al.*, "Contrast enhanced ultrasound by real-time spatiotemporal filtering of ultrafast images," *Phys. Med. Biol.*, vol. 62, no. 1, p. 31–42, Dec. 2016.

[9] D. H. Pham *et al.*, "The performance improvement of ultrasound localization microscopy (ulm) using the robust principal component analysis (rpca)," in *2023 45th IEEE Engineering in Medicine & Biology Society (EMBC)*, Jul. 2023, p. 1–4.

[10] K. Xu *et al.*, "Robust pca-based clutter filtering method for super-resolution ultrasound localization microscopy," in *2021 IEEE International Ultrasonics Symposium (IUS)*. IEEE, Sep. 2021, p. 1–4.

[11] R. R. Wildeboer *et al.*, "Blind source separation for clutter and noise suppression in ultrasound imaging: Review for different applications," *IEEE Trans. Ultrason. Ferroelectr. Freq. Control*, vol. 67, no. 8, pp. 1497–1512, 2020.

[12] V. Pustovalov *et al.*, "Computational super-resolution for ultrasound localization microscopy through solving an inverse problem," *IEEE Trans. Ultrason. Ferroelectr. Freq. Control*, vol. 72, no. 5, 2025.

[13] D.-H. Pham *et al.*, "Joint blind deconvolution and robust principal component analysis for blood flow estimation in medical ultrasound imaging," *IEEE Trans. Ultrason. Ferroelectr. Freq. Control*, vol. 68, no. 4, p. 969–978, Apr. 2021.

[14] X. Liu *et al.*, "Deep learning for ultrasound localization microscopy," *IEEE Trans. Med. Imaging*, vol. 39, no. 10, pp. 3064–3078, 2020.

[15] C. Hahne *et al.*, "Rf-ulm: Ultrasound localization microscopy learned from radio-frequency wavefronts," *IEEE Trans. Med. Imaging*, vol. 43, no. 9, pp. 3253–3262, 2024.

[16] X.-H. Le *et al.*, "BSRPCA: A Simplified Blind Super-Resolved RPCA-Based Approach for Enhancing Blood Flow Estimation," in *IEEE International Conference on Image Processing*, 2025, paper ID: 1899.

[17] T. Bouwmans and E. H. Zahzah, "Robust pca via principal component pursuit: A review for a comparative evaluation in video surveillance," *Comput. Vis. Image Underst.*, vol. 122, p. 22–34, May 2014.

[18] D.-H. Pham *et al.*, "Fast high resolution blood flow estimation and clutter rejection via an alternating optimization problem," in *2021 IEEE 18th International Symposium on Biomedical Imaging (ISBI)*. IEEE, Apr. 2021, p. 1907–1910.

[19] T. Lin *et al.*, "On the global linear convergence of the admm with multiblock variables," *SIAM J. Optim.*, vol. 25, no. 3, 2015.

[20] N. Zhao *et al.*, "Fast single image super-resolution using a new analytical solution for l2-l2 problems," *IEEE Trans. Image Process.*, vol. 25, no. 8, p. 3683–3697, Aug. 2016.

[21] W. W. Hager, "Updating the inverse of a matrix," *SIAM Review*, vol. 31, no. 2, pp. 221–239, Jun. 1989.

[22] Z. Lin *et al.*, "The augmented lagrange multiplier method for exact recovery of corrupted low-rank matrices," *CoRR*, 2010.

[23] J.-F. Cai *et al.*, "A singular value thresholding algorithm for matrix completion," *SIAM J. Optim.*, vol. 20, no. 4, pp. 1956–1982, 2010.

[24] A. Rodriguez-Molares *et al.*, "The generalized contrast-to-noise ratio: A formal definition for lesion detectability," *IEEE Trans. Ultrason. Ferroelectr. Freq. Control*, vol. 67, no. 4, pp. 745–759, 2020.

[25] O. Michailovich *et al.*, "Iterative reconstruction of medical ultrasound images using spectrally constrained phase updates," in *Proc. IEEE 16th Int. Symp. Biomed. Imag. (ISBI)*, April 2019, pp. 1765–1768.